Published in final edited form as:
J Nonnewton Fluid Mech. 2013 December 1; 202: 88–98. doi:10.1016/j.jnnfm.2013.09.010.

Gravity-Driven Thin Film Flow of an Ellis Fluid

Vitaly O. Kheyfets[a,1] and **Sarah L. Kieweg**[a]

Vitaly O. Kheyfets: vitaly.kheyfets@ucdenver.edu; Sarah L. Kieweg: kieweg@ku.edu

[a]Department of Mechanical Engineering, University of Kansas, 1530 W. 15th Street, 3138 Learned Hall, Lawrence, KS 66045

Abstract

The thin film lubrication approximation has been studied extensively for moving contact lines of Newtonian fluids. However, many industrial and biological applications of the thin film equation involve shear-thinning fluids, which often also exhibit a Newtonian plateau at low shear. This study presents new numerical simulations of the three-dimensional (i.e. two-dimensional spreading), constant-volume, gravity-driven, free surface flow of an Ellis fluid. The numerical solution was validated with a new similarity solution, compared to previous experiments, and then used in a parametric study. The parametric study centered around rheological data for an example biological application of thin film flow: topical drug delivery of anti-HIV microbicide formulations, e.g. hydroxyethylcellulose (HEC) polymer solutions. The parametric study evaluated how spreading length and front velocity saturation depend on Ellis parameters. A lower concentration polymer solution with smaller zero shear viscosity (η_0), $\tau_{1/2}$, and λ values spread further. However, when comparing *any* two fluids with any possible combinations of Ellis parameters, the impact of changing one parameter on spreading length depends on the direction and magnitude of changes in the other two parameters. In addition, the isolated effect of the shear-thinning parameter, λ, on the front velocity saturation depended on $\tau_{1/2}$. This study highlighted the relative effects of the individual Ellis parameters, and showed that the shear rates in this flow were in both the shear-thinning and plateau regions of rheological behavior, emphasizing the importance of characterizing the full range of shear-rates in rheological measurements. The validated numerical model and parametric study provides a useful tool for future steps to optimize flow of a fluid with rheological behavior well-described by the Ellis constitutive model, in a range of industrial and biological applications.

Keywords

thin film; lubrication approximation; Ellis fluid; microbicide; shear-thinning

1. Introduction

The thin film equation, obtained using the lubrication approximation, has been studied extensively for moving contact lines (e.g. [1, 2]) and for many applications and flow configurations. Applications with a free surface include spin-coating [3], biological flows [4,

Correspondence to: Sarah L. Kieweg, kieweg@ku.edu.

[1]Present address: Department of Bioengineering, University of Colorado, Denver

5, 6, 7, 8, 9], geophysical flows [10], bubbles moving in fluid-filled tubes [11], and pulling a plate from a fluid source (Landau-Levich problem) [12]. Most thin film flow studies have focused on Newtonian fluids. However, most industrial and biological applications involve non-Newtonian fluids, such as spin-coating, geophysical flows, tear film flow, and topical drug delivery. A subset of thin film flow studies have examined non-Newtonian behavior, with most focusing on the shear-thinning behavior (e.g. [13]) or yield stress (e.g. [14]). In a previous study [4], we used a 2D model of gravity and surface tension driven flow to examine the effect of power-law shear-thinning on the capillary ridge that is associated with a fingering instability at the moving front. Here, in this study, we derive a gravity-driven 3D model without surface tension to focus on how Ellis fluid parameters (including shear-thinning) impact spreading length and front speed saturation.

Thin film flow equations for Newtonian fluids have been extensively studied (e.g. [1, 2]), but are less common for non-Newtonian fluids (e.g. [13]) or more complex materials (e.g. [15]). Power-law and Ellis relationships are popular constitutive equations used to represent the shear-thinning (or shear-thickening) behavior of non-Newtonian fluids. The power-law and Ellis constitutive equations both allow straightforward analytical manipulation of terms during derivation of the thin film equation [3, 16]. In a previous study, we presented a 3D model of a power-law fluid in a gravity-driven, free surface flow configuration, and validated the model with experiments [17]. However, the power-law representation does not capture the Newtonian plateau behavior present in most polymeric solutions at low shear rates [16]. Since gravity-driven thin film flows of viscous fluids may have large regions of low shear rates, the Newtonian plateau may have a strong influence on spreading. Whether a particular flow is dependent on shear-thinning effects depends on whether the characteristic shear rate of that flow is in the Newtonian plateau range. For example, de Souza Mendes et al. [18] assume that shear-thinning effects are not important in thin films of thixotropic fluids coating the inside of a tube. The Ellis constitutive model uses three parameters to capture both the Newtonian plateau and the shear-thinning behavior. While similar to the power-law fluid in its analytical tractability, the Ellis model has small disadvantages associated with using three parameters (increased optimization/parametric space) and the inability to explicitly write an analytical solution to the thin film equation for the free surface height using the form of the characteristics (a numerical approximation is described in this paper). Shear-thinning constitutive relationships, such as power-law and Ellis, also present additional numerical challenges for 3D models because the constitutive forms result in additional spatial derivatives in each flux expression, which will also be described in this paper.

A few studies have examined Ellis fluids with the lubrication approximation using numerical or analytical approaches in several flow configurations, including: axisymmetric spin-coating with centrifugal forces [3], draining down a vertical wall with gravity and surface tension [19], spreading of tear substitutes during blinking under negligible gravity [5], spreading of tear films on curved substrates [20], a film of fluid on a plane withdrawn from a fluid source (Landau-Levich problem) [12, 11], and a gas bubble displacing liquid in a tube [11]. With the exception of the axisymmetric spin-coating, all of these have been 2D (i.e. 1D spreading) and with a constant flux of fluid. We are interested in a constant volume of fluid, and the 3D flow due to gravity. A 2D model cannot represent the lateral spreading

of a fixed volume of fluid, and will overestimate the downslope spreading. Thus, for constant volume flow, a 3D model is needed to examine how the Ellis parameters impact spreading.

While the previous studies of Ellis thin film flows were for different flow conditions than this study, they have indicated that shear-thinning had an impact on flow outcomes in those configurations. The only one with a constant volume, Charpin et al. [3], presented an axisymmetric thin film flow of spin-coating with centrifugal forces, gravity, and surface tension. With the influence of centrifugal force, they found that increased shear-thinning (in both Ellis and power-law fluids) increased spreading in the spin-coating flow. In the axisymmetric flow, they show that Ellis has benefits over power-law because of the zero shear behavior at the center of the flow.

The study by Weidner and Schwartz [19] was also closely related to the focus of this study, because it described gravity-driven flow of an Ellis fluid down a vertical wall. With the inclusion of surface tension, that study showed, as we did for a power-law fluid [4], that the capillary ridge height decreased with increased shear-thinning. However, Weidner and Schwartz [19] used a steady state analysis of a constant flux of fluid. Thus, while that study could focus on the steady velocity of the moving front and the shape of the capillary ridge, it did not examine the spreading length nor how the velocity of the moving front saturates.

Jossic et al. [5] modelled an eyelid sweeping across the eye and moving a thin film of tears under negligible gravity. While a different flow configuration, they showed that shear-thinning with Ellis parameters had an impact on film depth in all cases considered. Other studies have shown that for a residual film on a plane removed from a fluid bath, increased shear-thinning (for both power-law and Ellis fluids) reduced the residual film thickness [12, 11].

The aforementioned studies reveal a knowledge gap in thin film flow studies of Ellis fluids. Specifically, there are no previous thin film flow studies of 3D, constant volume, gravity-driven flows of shear-thinning fluids with a Newtonian plateau. Such a study is needed, as it will allow the parametric study for this flow configuration, and ultimately allow design of fluid properties for targeted spreading behavior. The previous studies in this field in different flow configurations, summarized above, indicate that the Ellis parameters are expected to have an impact on flow behavior in this new model. Thus, *the overall objective of this study* was to develop and validate a 3D numerical solution of a gravity-driven thin film flow of a constant volume of Ellis fluid, and use the model to answer the following questions:

- How does spreading length depend on the Ellis parameters? Specifically, how does shear-thinning impact spreading length, and is this dependent on the other Ellis parameters? This question is important because the outcome will allow for the design of a fluid with a target coating behavior, and is applicable to many industrial and biological applications.
- How much does the spreading velocity deviate from a steady velocity, and how does that depend on the Ellis parameters? This is important because it indicates

whether the spreading of the fluid has saturated, and no longer improving coverage. This new model allows for the examination of the changing velocity of the gravity-driven flow, which has not previously been studied for a constant volume of an Ellis fluid.

- What are the typical shear rates occurring in these thin film flows of Ellis fluids? Do the shear rates occur in the shear-thinning region or primarily in the Newtonian plateau regime? The outcome of this question will indicate the range of rheological data needed to characterize fluids in these flow configurations.

The following sections present the problem formulation, the numerical methods, validation, and a parametric study. We derive the thin film equation describing the evolving shape of the Ellis fluid's free surface, as a function of space and time, during gravity-driven flow. We present a numerical solution for the 3D equation, and validation with a similarity solution and our previously published experimental results [17]. The parametric study was oriented around an example application of interest to our research group – the drug delivery of microbicidal polymer solutions [21] to the vaginal epithelium for protection against HIV transmission. Microbicides can contain a pharmaceutical agent in a delivery vehicle, such as a film [22] or polymer solution (often referred to as a "gel" by the microbicide research community [21]). The computational model and results presented here provide a needed tool for optimizing non-Newtonian coating flows, for microbicidal drug delivery, as well as the other biological and industrial applications described above.

2. Methods

2.1. Problem Formulation

In this study, we derive the thin film equation for an Ellis fluid flowing in two directions under the influence of gravity (x – downslope and y – lateral directions). With surface tension neglected, the thin film equation is a second-order nonlinear partial differential equation describing the evolution of the free surface as a function of time and space, $h(x, y, t)$. Figure 1 shows the coordinate system diagram of the 3D flow.

We start with the conservation of linear momentum (Eq. 1):

$$\frac{\partial \mathbf{u}}{\partial t}+(\mathbf{u}\cdot\nabla)\,\mathbf{u}=-\frac{1}{\rho}\nabla p+\frac{1}{\rho}\nabla\cdot\boldsymbol{\tau}+\mathbf{g} \quad (1)$$

where $\mathbf{u}$ and $\mathbf{g}$ are the velocity and gravity vectors respectively, $\boldsymbol{\tau}$ is the viscous stress tensor, p is the pressure, and ρ is the density. Using the thin-film lubrication approximation [23], the momentum equation reduced to the following equations of motion in the x-, y-, and z-directions:

$$0=-\frac{\partial \rho}{\partial x}+\frac{\partial \tau_{zx}}{\partial z}+\rho g\sin\alpha \quad (2)$$

$$0=-\frac{\partial \rho}{\partial y}+\frac{\partial \tau_{zy}}{\partial z} \quad (3)$$

$$0=-\frac{\partial \rho}{\partial z}-\rho g\cos\alpha \quad (4)$$

where α is the inclination angle with respect to the horizontal plane (see Figure 1). Integration of the z-momentum equation (Eq. 4), along with a pressure condition on the free surface, $p|_{(z=h)} = p_0$, provided expressions for $\partial p/\partial x$ and $\partial p/\partial y$. In this study, we do not include surface tension in the pressure expression. The objectives of this study are focused on the 3D spreading and Ellis parameter effects, rather than the combined effects of surface tension and shear-thinning, which we previously examined with a 2D power-law shear-thinning model [4]. The expected impact of surface tension is discussed later.

The Ellis constitutive equation [24]:

$$\frac{1}{\eta}=\frac{1}{\eta_0}\left(1+\left|\frac{\mathrm{II}_\tau}{\tau_{1/2}}\right|^{\lambda-1}\right) \quad (5)$$

relates the viscosity η to the second invariant of the viscous stress tensor, $\mathrm{II}_\tau=\sqrt{\tau_{zx}^2+\tau_{zy}^2}$, where η_0 is the zero-shear viscosity, λ is the measure of shear-thinning behavior ($\lambda > 1$ is shear-thinning), and $\tau_{1/2}$ is the shear stress at which the apparent viscosity has dropped to half its zero-shear viscosity value.

The relevant shear stress components of the viscous stress tensor were:

$$\tau_{zx}=\eta\frac{\partial u}{\partial z} \quad (6)$$

and

$$\tau_{zy}=\eta\frac{\partial v}{\partial z} \quad (7)$$

where u and v were the velocities in the x and y directions, respectively. These expressions were combined with the Ellis constitutive equation (Eq. 5) and expressions for τ_{zx} and τ_{zy} obtained from integrating the x and y equations of motion (Eqs. 2 and 3) using the free surface boundary conditions: $\tau_{zx}|_{(z=h)} = \tau_{zy}|_{(z=h)} = 0$. Using the no-slip boundary conditions, $u|_{z=0} = v|_{z=0} = 0$, we obtained expressions for velocity in the downslope direction, $u(x, y, z, t)$, and lateral direction, $v(x, y, z, t)$:

$$u=\left(\frac{\rho g}{\eta_0}\right)\left(\frac{\partial h}{\partial x}\cos\alpha-\sin\alpha\right)\left[\frac{1}{2}z^2-hz+\left(\frac{\sqrt{A}}{\tau_{1/2}}\right)^{\lambda-1}\left(\frac{1}{\lambda+1}\right)\left\{(h-z)^{\lambda+1}-(h)^{\lambda+1}\right\}\right] \quad (8)$$

$$v=\left(\frac{\rho g}{\eta_0}\right)\left(\frac{\partial h}{\partial y}\cos\alpha\right)\left[\frac{1}{2}z^2-hz+\left(\frac{\sqrt{A}}{\tau_{1/2}}\right)^{\lambda-1}\left(\frac{1}{\lambda+1}\right)\{(h-z)^{\lambda+1}-(h)^{\lambda+1}\}\right] \quad (9)$$

where

$$A=(\rho g)^2\left[\left(\frac{\partial h}{\partial x}\cos\alpha-\sin\alpha\right)^2+\left(\frac{\partial h}{\partial y}\cos\alpha\right)^2\right] \quad (10)$$

Equation 8 corresponds to the equation for u for an Ellis fluid in Myers [16] (Eq. 9 in that study) if consider only the x-direction, and neglect $\cos\alpha\frac{\partial h}{\partial x}$ (i.e. relatively steep or vertical inclines). The flow rates per unit width (flux), in the downslope and lateral directions, q_x and q_y, were found with the following expressions:

$$q_x=\int_0^{h(x,y,t)}u(x,y,z,t)dz \quad (11)$$

$$q_y=\int_0^{h(x,y,t)}v(x,y,z,t)dz \quad (12)$$

This resulted in the following equations for flow rate per unit width in the downslope and lateral directions:

$$q_x=\left(\frac{\rho g\cos\alpha}{\eta_0}\right)\left(\tan\alpha-\frac{\partial h}{\partial x}\right)\left[\frac{h^3}{3}+\left(\frac{\rho g\cos\alpha}{\tau_{1/2}}\right)^{\lambda-1}\left(\frac{1}{\lambda+2}\right)\{B\}^{\frac{\lambda-1}{2}}h^{\lambda+2}\right] \quad (13)$$

$$q_y=\left(\frac{\rho g\cos\alpha}{\eta_0}\right)\left(\frac{\partial h}{\partial x}\right)\left[\frac{h^3}{3}+\left(\frac{\rho g\cos\alpha}{\tau_{1/2}}\right)^{\lambda-1}\left(\frac{1}{\lambda+2}\right)\{B\}^{\frac{\lambda-1}{2}}h^{\lambda+2}\right] \quad (14)$$

where

$$B=\left(\tan\alpha-\frac{\partial h}{\partial x}\right)^2+\left(\frac{\partial h}{\partial y}\right)^2 \quad (15)$$

Incorporating the flux expressions (Eqs. 13 and 14) into the conservation of mass resulted in the second order partial differential equation describing the evolution of the free surface, $h(x, y, t)$, of an Ellis fluid:

$$\frac{\partial h(x,y,t)}{\partial t}+\frac{\partial q_x}{\partial x}+\frac{\partial q_y}{\partial y}=0 \quad (16)$$

The 3D Newtonian evolution equation (see e.g., Eq. 3 without surface tension in Ref. [25]) is recovered from the Ellis evolution equation (Eq. 16) when $(\tau_{1/2})^{1-\lambda}\to 0$ [5]. However, in

the 3D model, there is a distinctive difference between shear-thinning and Newtonian evolution equations, which requires additional numerical discretization decisions. Each of the flux expressions in the Ellis evolution equation contain both $\partial h/\partial x$ and $\partial h/\partial y$ terms. In contrast, the Newtonian form only contains the corresponding derivative in each flux expression (i.e. $\partial h/\partial x$ only occurs in the q_x expression). The numerical discretization of the Ellis evolution equation is described later in Section 2.2.

To reduce the evolution equation to a non-dimensional form, the following scalings were used: $h' = h/H$, $x' = x/H$, $y' = y/H$, and $t' = t/T$, where H was the initial maximum height of the free surface, and T was determined after scaling the evolution equation (Eq. 16). Substitution of those scalings into the evolution equation yielded the following non-dimensional groupings (in addition to the non-dimensional shear-thinning parameter, λ):

$$E' = \frac{\rho g H \cos\alpha}{\tau_{1/2}} \quad (17)$$

$$t' = \frac{t}{T} = \frac{t}{\left(\frac{\eta_0}{\rho g H \cos\alpha}\right)} \quad (18)$$

E' represents the ratio of normal gravity effects to the Ellis parameter, $\tau_{1/2}$, similar to Ellis non-dimensional groupings used for steady state analysis by Afanasiev et al. [12] for the Landau-Levich problem and Weidner and Schwartz [19] for steady flow down a vertical wall. The t' grouping represents the ratio of normal gravity to viscous terms. The nondimensional evolution equation becomes:

$$\frac{\partial h'(x,y,t)}{\partial t'} + \frac{\partial q'_{x'}}{\partial x'} + \frac{\partial q'_{y'}}{\partial y'} = 0 \quad (19)$$

with

$$q'_{x'} = \left(\tan\alpha - \frac{\partial h'}{\partial x'}\right) \left[\frac{h'^3}{3} + (E')^{\lambda-1} \left(\frac{1}{\lambda+2}\right) \{B'\}^{\frac{\lambda-1}{2}} h'^{\lambda+2}\right] \quad (20)$$

$$q'_{y'} = \left(\frac{\partial h'}{\partial y'}\right) \left[\frac{h'^3}{3} + (E')^{\lambda-1} \left(\frac{1}{\lambda+2}\right) \{B'\}^{\frac{\lambda-1}{2}} h'^{\lambda+2}\right] \quad (21)$$

and B' is a dimensionless version of B (Eq. 15). Note that the evolution equation is now only a function of E' and λ, and the effects of viscosity, η_0, scale with t'.

2.2. Numerical Methods and Validation

The free surface evolution equation (Eq. 16) was solved numerically for $h(x, y, t)$ using an implicit 3-nite difference scheme which was second order in both space and time, as

described in this section. The numerical domain on the inclined spreading surface in the *x*-*y* plane (see Figure 1) was uniformly divided into rectangular grid points, $N \cdot M$, in the *x* and *y* directions, respectively (see Figure 2). The $N \cdot M$ grid points were indexed 0 to $N \cdot M - 1$ using a *k* indicial notation, as shown in the computational stencil in Figure 2. The Δx and Δy grid sizes were uniform in each direction, but not required to be equal. The domain size dynamically expanded over time to accommodate the spreading fluid and improve computational performance. Therefore, *N* and *M* were not fixed values, but instead constantly growing throughout the simulation. For example, at the beginning of a simulation ($t = 0s$), the computational domain was divided into 400 (*N*) × 300 (*M*) nodes. Because $\Delta x = \Delta y = 0.01cm$ was chosen for all simulations (determined after a mesh convergence study, described later in this section), the result was a spreading surface of 4.0 × 3.0 *cm*. At $t = 10s$, the contact line started to approach the 4 *cm* boundary, therefore N was automatically increased to 450 to adapt the computational domain to 4.5 *cm*. In this method, the downslope and lateral contact lines never reached the domain boundaries, and *h* remained zero at and near the boundaries.

The spatial derivatives of the flux terms in the evolution equation (Eq. 16) were discretized using central difference approximations as follows (refer to the computational stencil in Figure 2):

$$\left(\frac{\partial q_x}{\partial x}\right)_k = \frac{(q_x)_{k+M_{1/2}} - (q_x)_{k-M_{1/2}}}{\Delta x} \quad (22)$$

$$\left(\frac{\partial q_y}{\partial y}\right)_k = \frac{(q_y)_{k+1/2} - (q_y)_{k-1/2}}{\Delta y} \quad (23)$$

where the $k \pm M_{1/2}$ indicial notation indicates the temporary designation of the flux at the node interfaces between the *k*, $k + M$, and $k - M$ grid nodes; similar notation is used for $k \pm 1/2$ (also used in Ref. [18]). The spatial derivatives of *h* within the flux equations (see Eqs. 13 and 14) were further discretized using central differences centered about the node interfaces as follows:

$$(q_x)_{k+M_{1/2}} = \left(\frac{\rho g \cos\alpha}{\eta_0}\right) \left(\tan\alpha - \frac{h_{k+M} - h_k}{\Delta x}\right) * \left[\frac{1}{3}\frac{h_k^3 + h_{k+M}^3}{2} + C\left(\left(\tan\alpha - \frac{h_{k+M} - h_k}{\Delta x}\right)^2 + \left(\frac{\partial h}{\partial y}\right)^2\right)^{\frac{\lambda-1}{2}} \left(\frac{h_k^{\lambda+2} + h_{k+M}^{\lambda+2}}{2}\right)\right] \quad (24)$$

$$(q_x)_{k-M_{1/2}} = \left(\frac{\rho g \cos\alpha}{\eta_0}\right) \left(\tan\alpha - \frac{h_k - h_{k-M}}{\Delta x}\right) * \left[\frac{1}{3}\frac{h_k^3 + h_{k-M}^3}{2} + C\left(\left(\tan\alpha - \frac{h_k - h_{k-M}}{\Delta x}\right)^2 + \left(\frac{\partial h}{\partial y}\right)^2\right)^{\frac{\lambda-1}{2}} \left(\frac{h_k^{\lambda+2} + h_{k-M}^{\lambda+2}}{2}\right)\right] \quad (25)$$

$$(q_y)_{k+1/2} = -\left(\frac{\rho g \cos\alpha}{\eta_0}\right)\left(\frac{h_{k+1}-h_k}{\Delta y}\right) * \left[\frac{1}{3}\frac{h_k^3+h_{k+1}^3}{2} + C\left(\left(\tan\alpha - \frac{\partial h}{\partial x}\right)^2 + \left(\frac{h_{k+1}-h_k}{\Delta y}\right)^2\right)^{\frac{\lambda-1}{2}}\left(\frac{h_k^{\lambda+2}+h_{k+1}^{\lambda+2}}{2}\right)\right] \quad (26)$$

$$(q_y)_{k-1/2} = -\left(\frac{\rho g \cos\alpha}{\eta_0}\right)\left(\frac{h_k-h_{k-1}}{\Delta y}\right) * \left[\frac{1}{3}\frac{h_k^3+h_{k-1}^3}{2} + C\left(\left(\tan\alpha - \frac{\partial h}{\partial x}\right)^2 + \left(\frac{h_k-h_{k-1}}{\Delta y}\right)^2\right)^{\frac{\lambda-1}{2}}\left(\frac{h_k^{\lambda+2}+h_{k-1}^{\lambda+2}}{2}\right)\right] \quad (27)$$

where

$$C = \left(\frac{\rho g \cos\alpha}{\tau_{1/2}}\right)^{\lambda-1}\left(\frac{1}{\lambda+2}\right) \quad (28)$$

The discretization for the $h^{\lambda+2}$ expressions in the gravity terms at the end of the flux equations is the shear-thinning version of the discretization used by Kondic and Diez for the Newtonian gravity h^3 expression for a Newtonian fluid [2, 26].

The remaining derivatives of h, which are not yet discretized in the above equations, include the dh/dy terms in both of the downslope flux equations, and the dh/dx terms in both of the lateral flux equations. As noted earlier, these additional h derivatives do not occur in the 3D Newtonian evolution equation, and are a distinctive aspect of the Ellis and power-law 3D evolution equations. This distinguishing feature of the shear-thinning 3D equations requires a decision on the appropriate computational stencil for the additional derivatives such that the fluid volume is conserved. Thus, we discretized these additional derivatives as shown in our previous study for a power-law fluid (Eqs. 18–21 of [17]) and confirmed volume was conserved. This technique extended the 5-point computational stencil of a Newtonian computation [25] to an eight-point computational stencil (see Figure 2), increasing the computational expense.

The evolution equation, Eq. 16, was discretized in time using a Θ-scheme [2]:

$$\frac{h_k^{p+1}-h_k^p}{\Delta t} + \Phi f_k^{p+1} + (1-\Theta) f_k^p = 0 \quad (29)$$

where $f^p = f(h^p)$ is defined from the evolution equation as:

$$f_k^p = \left(\frac{\partial q_x}{\partial x}\right)_k^p + \left(\frac{\partial q_y}{\partial y}\right)_k^p \quad (30)$$

where $h^p = h(x, t^p)$, p is the time index, and $\Theta = 1/2$, which provided a second-order accurate, implicit, Crank-Nicholson scheme. The result was $N \cdot M$ nonlinear equations with $N \cdot M$ unknowns:

$$F_k\left(h_k^{p+1}, h_{k+M+1}^{p+1}, h_{k-M+1}^{p+1}, h_{k+1}^{p+1}, h_{k-1}^{p+1}, h_{k+M}^{p+1}, h_{k-M}^{p+1}, h_{k+M-1}^{p+1}\right)=0 \quad \text{for} \quad 0 \leq k \leq N \cdot M-1 \tag{31}$$

The nonlinear system was solved using Newton's method, which was set to converge as the maximum change to the solution fell below 10^{-9}. At each iteration of Newton's method, the linear system was solved using a preconditioned biconjugate gradient method (considered converged as the maximum change to the solution fell below 10^{-6}), where the preconditioner was found using incomplete LU factorization of the Jacobian.

Fourth-order degenerate thin film equations, which include surface tension terms, do not satisfy the maximum principle [27]. The second-order degenerate thin film equation in this study does satisfy the maximum principle [1], and a precursor was not required. However, false nonpositive numerical solutions can still occur [27], and at these locations, we employed a simple positivity preserving scheme which detected the occasional small nonpositive solutions and set those values to $h = 0$. Volume was monitored and confirmed to be conserved with this scheme.

A time-adaptation scheme was used to improve computational efficiency. If either Newton's or the biconjugate gradient method did not converge within a threshold of iterations, the time step was decreased and the step was repeated. If the method did converge within a specified number of iterations, the time step was gradually increased. This provided much improved computation times, with the same accuracy. For example, a 90-second simulation required about 5 days of computation, as opposed to 30 days for a simulation continuously computed at a time step of $2.5 \cdot 10^{-4}s$. Three-dimensional numerical solutions of the Newtonian thin film equation are known to be computationally expensive [26, 28], and based on our previous work with 2D simulations of power-law fluids with surface tension [4], we expected the simulation times required in this shear-thinning, 3D study.

The numerical methods were validated with volume conservation, convergence, comparison to a similarity solution, and comparison to experiments. Volume was monitored during all simulations and conserved within 0.001% over the entire simulation time. A mesh convergence study showed spatial mesh convergence in the downslope and lateral directions for a Newtonian case. Following the mesh convergence study, we selected a $\Delta x = \Delta y = 0.01cm$ for all simulations in this study, which provided a reasonable computation time.

The similarity solution was found by considering the 2D version of the 3D Ellis evolution equation (Eq. 16) at very steep inclination angles ($\cos\alpha \frac{\partial h}{\partial x} \ll 0$):

$$\frac{\partial h}{\partial t}+\frac{\rho g \sin\alpha}{\eta_0}\left[h^2+\left(\frac{\rho g \sin\alpha}{\tau_{1/2}}\right)^{\lambda-1} h^{\lambda+1}\right]\frac{\partial h}{\partial x}=0 \tag{32}$$

Using the method of characteristics (as outlined by Huppert [29] for a Newtonian fluid), we considered a constant h along characteristics described by:

$$\frac{dx}{dt}=\frac{\rho g\sin\alpha}{\eta_0}\left[h^2+\left(\frac{\rho g\sin\alpha}{\tau_{1/2}}\right)^{\lambda-1}h^{\lambda+1}\right] \quad (33)$$

This equation is used to write an analytical expression for the equation of characteristics given by $x(t)$. For Newtonian [27] and power-law fluids [4], the equation of the characteristics, $x(t)$ is used to write an analytical expression for $h(x, t)$ when $x \gg x_0$, the initial value of the characteristic. However, for the Ellis fluid, the form of the characteristics (which include separate h^2 and $h^{\lambda+1}$ terms) does not allow one to write an explicit expression for $h(x, t)$. Therefore, Newton's method was used to solve for h at discrete points along the x-axis, at a given time. The convergence criterion for Newton's method was considered satisfied when the maximum change to the solution fell below 10^{-6}.

The numerical solution of the full Ellis evolution equation was also compared to previously published experiments and a numerical solution representing only the shear-thinning behavior (power-law). [17]

2.3. Parametric Study

For all simulations in the parametric study, the initial shape was described by $h = H\,(-x^4 - y^4 + 1)$, which prescribed the initial length, L, and width W of the footprint, where H was the initial maximum height. For all dimensional simulations in this study, $H = 0.5cm$, $L = 2cm$, $W = 2cm$, and the inclination angle was $\alpha = 30\,°$. For the dimensional study, we selected Ellis rheological parameters relevant to our application of interest – anti-HIV microbicidal polymer solutions. An example is the hydroxyethylcellulose (HEC) used in the Universal Placebo for microbicide clinical trials [21]. Figure 3 presents example rheological data for three concentrations of HEC solutions, centered around the recipe for the 2.7% HEC used in the Universal Placebo. At these concentrations and stresses, the fluids exhibited a Newtonian plateau at low shear rates, suggesting the use of the Ellis model. The Ellis parameters (using Eq. 5) for these gels are shown in Table 1. Using these example gels, we selected the following ranges for a parametric study: η_0: $1200 - 3200P$, $\tau_{1/2} = 200 - 800dyn/cm^2$, and λ: 1.2 – 3.

In this study, we present both dimensionless and dimensional results. For constant volume applications (as opposed to a constant-flux source of fluid), the dimensional effects of the Ellis parameters on spreading behavior are of interest and those results are most easily viewed through a dimensional parametric study (see e.g. [4]). In addition, the dimensional analysis is relevant to experimental comparisons and for future studies in the optimization of the rheological properties for target spreading behavior (e.g. in microbicidal gel delivery).

3. Results and Discussion

Figure 4 shows a typical numerical result for the 3D spreading of an example Ellis fluid parameter set. The figure indicates both the evolution of a centerline side-view and the final footprint with height contours indicated. The figure indicates both convective and diffusive spreading in the downslope direction, and diffusive spreading in the lateral direction, to

create a footprint with a narrowing width near the moving front. The free surface slope is steepest at the moving contact line and a steep slope may be a limitation to the lubrication approximation. (Note the free surface slope is exaggerated in Figure 4 because the axes are scaled differently.) The limitation of the steep slope at the contact line is acknowledged in lubrication approximation literature [25, 30], but the thin film equation is still known to be successful for comparisons to experiments and analysis [30].

The solutions for $h(x, y, z, t)$ were also used to estimate the shear rates throughout the fluid volume using expressions for $\partial u/\partial z$ and $\partial u/\partial z$. The computed shear rates from these simulations overlapped the shear rate ranges of both the Newtonian plateau and shear-thinning rheological behavior for these Ellis fluids (see Figure 3). In addition to low calculated shear rates in the Newtonian plateau region, the fluid experienced shear rates of over 0.1/s at many spatial locations even at later times, and some regions exceeded 1/s at earlier times (data not shown).

As a validation of the numerical methods, we confirmed that the numerical solution approaches the similarity solution at long times. Figure 5 shows an example of a side profile at the centerline of the 3D numerical solution compared with the 2D similarity solution at two times, for a given set of parameters. The simulation was of a very steep incline to match the assumptions of the similarity solution, and this resulted in a sharp moving front as expected. These results indicated that the numerical solution approached the similarity solution as $t \to \infty$.

The numerical simulations were also compared to our previously published experimental results and simulations of a power-law fluid (i.e. the Newtonian plateau was not represented) [16]. In that previous work, we presented a method to obtain the 3D shape of the free surface of a spreading fluid during an experiment, utilized the experimental surface topography as the numerical initial shape, and compared spreading between power-law simulations and corresponding experiments of HEC polymer solutions.

Figure 6 presents the downslope spreading length for nine experiments compared against corresponding numerical simulations. The experimentally-obtained shape of the free surface of each experiment was used as input to the numerical simulations. Rheological parameters were obtained independently using rheometric data (i.e. Table 1 for the Ellis parameters in this study) and used as input to the numerical simulations. Qualitatively, the Ellis model was observed to improve agreement with experiment as compared to the power-law model. For quantitative comparison, Table 2 shows the RMS error comparing each simulation with experiment over 90 seconds. The Ellis simulations resulted in lower RMS errors for all nine experiments, as compared to the power-law simulations.

3.1. Spreading Length

Figure 7 presents a dimensional parametric study over the Ellis parameter space, and their influence on downslope spreading. It shows nine contour plots, with an outcome measure (spreading length at the front, L_f, at a given time) depicted over the parameter space described by the three Ellis parameters: λ, η_0, and $\tau_{1/2}$. We first focus on the dimensional values, to see the effects of each Ellis parameter within the range considered.

Figure 7 shows that the highest values of downslope spreading length occurred at the lowest values of all three Ellis parameters. For example, this study showed a comparison of fluids which varied only in HEC concentration. The fluid with the smallest Ellis parameters (i.e., the least HEC concentration had the lowest η_0, $\tau_{1/2}$, and λ) spread the furthest, as expected. However, when comparing *any* two fluids with any possible combinations of parameters, the impact of a decrease in one Ellis parameter on spreading length depends on the direction and magnitude of changes in the other two Ellis parameters. Thus, the parametric study results in Figure 7 provide a way to predict, compare, and optimize spreading behavior for given fluid rheological properties.

Using Figure 7, the effects of each individual Ellis parameter can be isolated. For a fixed λ and $\tau_{1/2}$, as η_0 is decreased the fluid will spread more, as expected. For a given η_0 and $\tau_{1/2}$, as the shear-thinning parameter(λ) approaches one (i.e. less shear-thinning), the fluid will also spread more. And, finally, if the other terms are constant, a drop in $\tau_{1/2}$ will also increase spreading. The non-dimensional plot (Figure 8) reveals the same trends by showing that dimensionless spreading is larger for increased E' and t' and decreased λ.

Additionally, Figure 7 also provides information on the relative impact of each parameter by comparisons of the general shapes of the contours. For example, the first row in Figure 7 shows that as λ is decreased (i.e. less shear-thinning), the contours are more linear and vertical over the $\tau_{1/2}$ and λ space. Those contour shapes indicate that changes in $\tau_{1/2}$ have little impact as λ is decreased. This result matches the expectation from the Ellis constitutive equation: as the fluid approaches Newtonian behavior, the viscosity (η_0) determines the flow behavior. The non-dimensional analysis (Figure 8) showed the same trend: as λ decreases, E' has less impact on spreading.

Similarly, the third row of Figure 7 indicates that the contours over the η_0 and λ space become more horizontal as $\tau_{1/2}$ decreases, suggesting that spreading becomes more independent of λ as $\tau_{1/2}$ decreases. This is easier to see in the non-dimensional figure (Figure 8), where λ has less impact as E' is increased.

The shape of the contour lines in the second row of Figure 7 yields information about the relative impact of $\tau_{1/2}$ and λ. The shape of the contour lines over the $\tau_{1/2}$ and λ space are not affected by different values of η_0, indicating that while η_0 impacts downslope spreading, it does not change the overall dependence of spreading on $\tau_{1/2}$ and λ. The non-dimensional analysis (Figure 8) confirms that relationship. As the η_0 is changed in the non-dimensional time, the relative dependence of the spreading length on λ and the non-dimensional E do not change; while, of course, the spreading length does change with changes in time and η_0. This also indicates that we expect to see the same trends shown in Figure 8 at later times.

3.2. Spreading Saturation

Figure 9 is another set of contour plots of a different outcome measure over the Ellis parameter space. Here, the outcome parameter is growth saturation, S, and is a measure of how the velocity of the moving front changes. We define a saturation parameter, S,

$$S=\frac{A_{L_f}-A_S}{A_S} \quad (34)$$

where A_{Lf} is the area under a L_{front} vs t curve (i.e. a deceleration, or a velocity saturation), and A_S is the area under a straight-line plot to reach the L_{front} value at the final time-point (i.e. constant velocity). Thus, saturation, S, represents the relative deviation of the L_f vs t curve from a constant velocity plot. For example, if the velocity of the spreading front was more constant, then the saturation approaches zero. If the front velocity was decelerating more, then the saturation value increases. Thus, S is a measure of front velocity saturation.

Figure 9 indicates that the highest values of S (i.e. less constant velocity and more saturation) occurred at the lowest values of η_0 and $\tau_{1/2}$. However, unlike for the spreading length values in Figure 7, the effect of changing λ alone on saturation depends on the $\tau_{1/2}$ value. This is evident in the second row of contours in Figure 9, where the effect of λ is different for lower and higher $\tau_{1/2}$: at higher $\tau_{1/2}$, increasing λ decreases saturation. Row three also shows the same effect: the shapes of the contours over the λ space change for different values of $\tau_{1/2}$ moving across the row of contour plots. The different trends for λ are clear in the non-dimensional plot (Figure 10): at smaller E', the dependence on λ is decreasing, while it is increasing at higher E'. This indicates that there may be a critical value for E' where the effect of λ is negligible on velocity saturation. In addition, the non-dimensional plots reinforce the trends for η_0 and $\tau_{1/2}$: as η_0 decreases (or as t' increases), the saturation levels increase, and as $\tau_{1/2}$ decreases (or as E' increases), the saturation also increases.

As observed for the spreading length, the shapes of the saturation contours in the first row of Figure 9 show that as λ decreases (i.e. less shear-thinning), the saturation is more independent of $\tau_{1/2}$. The non-dimensional plots (Figure 10) also show the same trend: E' has less impact at lower λ values. Again, this was expected since the viscosity effects should dominate for a more Newtonian fluid. Row two contours in Figure 9 are similar in shape across the row, and that indicates that as η_0 changes, the relative effects of the other two Ellis parameters are similar – as it was for spreading length. This is also seen in the non-dimensional plot (Figure 10) by noticing that the trends stay the same as t' changes. This indicates that trends at future time points will remain the same.

3.3. Discussion of Surface Tension and Wettability

This study did not consider surface tension, which would be expected to further slightly constrain the downhill gravity spreading (due to the gravity component parallel to the incline) and slumping behavior (due to gravity component perpendicular to the incline). Our previous study [4] on surface tension and gravity-driven flow examined the effects of shear-thinning on the formation of a capillary ridge in a 2D model. The capillary ridge is associated with the onset of lateral fingering instabilities [31]. Thus, ongoing studies in our research group are developing a 3D model with both surface tension and shear-thinning to examine the fingering patterns that emerge with an applied lateral perturbation. Such computational models are even more expensive than the present 3D model in this study, due to both the 4th-order terms in the thin film equation, and the discretization requirements for

the derivatives in the flux terms that arise due to the shear-thinning constitutive equations, as described in this study. Three-dimensional numerical simulations of fourth-order thin film equations for Newtonian fluids are known to be computationally expensive [26, 28], and thus, based on this study and our previous work [4], we know that the shear-thinning terms will increase computational needs. Thus, this study focused on the specific objectives stated in the Introduction, and the effects of shear-thinning on lateral fingering patterns are planned for future studies.

In the experiments of small volumes of very viscous fluids (results shown in Figure 6), we did not observe transverse fingering patterns at the advancing front. This observation actually matches intuition based on every day experiences with small ($<\approx 3mL$) "blobs" of typical viscous fluids in common use. However, we also expected that behavior based on linear stability analysis (LSA) of Newtonian fluids spreading on an incline. LSA also informs our expectations of the effect of including surface tension in this study's 3D Ellis computational model. LSA for Newtonian fluids indicates that instability at the contact line is stabilized by a stronger normal component of gravity [31, 32]. The dimensionless parameter $D(\alpha) = 3(Ca)^{1/3} \cot \alpha$ used in LSA represents the strength of the normal component of gravity [25]. The capillary number is typically defined as $Ca=\frac{\mu U}{\gamma}$ and includes the Newtonian viscosity (μ) and a velocity scale (U). Our experiments were on a relatively flat incline $\alpha = 30°$ and so we would expect the normal components of gravity to be strong in comparison to surface tension effects. As D increases (with flatter inclines or lower surface tension), LSA shows that there is typically an increased band of wave numbers in the stable region (see Fig 2c in [26]), and the stable region is no longer only at high wavenumbers (i.e. short wavelengths) as it is for $D = 0$. In other words, the mode of maximum unstable growth corresponds to longer wavelengths as D increases. However, these experiments with small volumes had transverse widths that were likely smaller than the longer wavelengths associated with maximum unstable growth. We are currently extending LSA to study the effects of shear-thinning and viscoelasticity (along with surface tension) on the contact line instability; for example, Spaid and Homsy [33] found that elastic effects tend to stabilize the capillary ridge.

Contact line motion is influenced by other factors such as wettability and surface roughness, and these represent ongoing challenges in thin film flow research [34]. Wettability of a fluid/solid interaction influences spreading behavior [35, 25, 36] and could be considered using the contact angle at the moving contact line. For example, stability analysis can be used in a slip model to understand the effect of contact angle on instabilities at the front; Spaid and Homsy [33] found the instability is not affected by contact angle for small contact angles. However, the numerical incorporation of contact angle (e.g. in a volume of fluid (VOF) model [35]) is restricted by the challenges of capturing the realistic variable contact angle [35], which is also a function of the front velocity [36]. Thus, this study's analysis of velocity saturation may inform future models incorporating dynamic contact angle, since the saturation of the front velocity depends on the Ellis parameters.

4. Conclusions

In this study, we presented new 3D simulations of constant-volume, gravity-driven, free surface flow of an Ellis fluid, using the thin film lubrication approximation. The numerical solution was validated with a new similarity solution, compared to previous experiments, and used in a parametric study to examine the effects of the three Ellis parameters on the spreading outcomes of length and front velocity saturation. The Ellis fluid simulations showed improved agreement with experiment as compared to the power-law model which did not represent the fluid's Newtonian plateau behavior. In addition, the simulation results indicate that the shear rates encountered in these simulations and experiments were in the regime of both shear-thinning and plateau regions of rheological data. This is an important outcome, particularly for the microbicide application, as it demonstrates the importance of collecting the full shear rate range of rheological data, which often requires a high-end rheometer.

Overall, for the presented parameter ranges, a lower concentration polymer solution with smaller η_0, $\tau_{1/2}$, and λ values is expected to flow with an increased spreading length, and that was confirmed in the experiments. However, when comparing *any* two fluids with any possible combinations of Ellis parameters, the impact of changing one parameter on spreading length depends on the direction and magnitude of changes in the other two parameters. The overall dependence on all three parameters again emphasizes the need to characterize rheological behavior over a full shear rate range.

The isolated effect of the shear-thinning parameter, λ, on the front velocity saturation will depend on the relative value of $\tau_{1/2}$; i.e. saturation depends on the magnitude of E'. This indicates a value for E' where the effect of λ has relatively little impact on saturation. For larger E' (i.e. normal gravity terms dominate the $\tau_{1/2}$ term), an increase in shear-thinning behavior causes more velocity saturation. When E' is smaller, indicating normal gravity is less influential than the $\tau_{1/2}$ term, the increased shear-thinning behavior reduces the velocity saturation. These results suggest the usefulness of a computational model to predict the flow of fluids with different Ellis parameters, under a particular flow configuration.

The parametric study indicated how changing one parameter may have little or more influence on spreading outcomes, and that the effect of that parameter depends on the other Ellis parameters. This will also be of importance when considering the effects of dilution [8] or formulation conditions on the change in parameters, and how sensitive a given polymer solution may be to changes in those parameters due to dilution or formulation conditions. Finally, an understanding of these relationships, provided by this numerical model, will be useful for predicting or optimizing the flow of a fluid with rheological behavior that is well-represented by the Ellis constitutive model, in a range of industrial and biological applications.

Acknowledgments

The project described was supported by NIH Grant Number R21/R33 AI082697 (from the National Institute of Allergy and Infectious Diseases) and NIH Grant Number KI2 HD052027 (from the National Institute of Child Health & Human Development). The content is solely the responsibility of the authors and does not necessarily represent the official views of the NIAID, NICHD, or the National Institutes of Health. Some of the computational

resources were funded by NSF MRI 0821625 for simulations run on the University of Kansas ITTC high-performance computing cluster. V.O.K. was also supported by NSF 07-555 GK-12. We gratefully acknowledge discussions with Md. Rajib Anwar and Bin Hu on topics related to this study.

References

1. Bertozzi A. The mathematics of moving contact lines in thin liquid films. Notices of the AMS. 1998:689–697.
2. Diez JA, Kondic L. Computing three-dimensional thin film flows including contact lines. Journal of Computational Physics. 2002; 183:274–306.
3. Charpin JPF, Lombe M, Myers TG. Spin coating of non-Newtonian fluids with a moving front. Physical Review E. 2007; 76
4. Hu B, Kieweg SL. The effect of surface tension on the gravity-driven thin film flow of Newtonian and power-law fluids. Computers & Fluids. 2012; 64:83–90. [PubMed: 23687391]
5. Jossic L, Lefevre P, de Loubens C, Magnin A, Corre C. The fluid mechanics of shear-thinning tear substitutes. Journal of Non-Newtonian Fluid Mechanics. 2009; 161:1–9.
6. Szeri AJ, Park SC, Verguet S, Weiss A, Katz DF. A model of transluminal flow of an anti-HIV microbicide vehicle: Combined elastic squeezing and gravitational sliding. Physics of Fluids. 2008; 20:083101–10.
7. Tasoglu S, Park SC, Peters JJ, Katz DF, Szeri AJ. The consequences of yield stress on deployment of a non-Newtonian anti-HIV microbicide gel. Journal of Non-Newtonian Fluid Mechanics. 2011; 166:1116–1122. [PubMed: 22563138]
8. Tasoglu S, Peters JJ, Park SC, Verguet S, Katz DF, Szeri AJ. The effects of inhomogeneous boundary dilution on the coating flow of an anti-HIV microbicide vehicle. Physics of Fluids. 2011; 23
9. Tasoglu S, Katz DF, Szeri AJ. Transient spreading and swelling behavior of a gel deploying an anti-HIV topical microbicide. Journal of Non-Newtonian Fluid Mechanics. 2012; 187188:36–42. [PubMed: 23425996]
10. Balmforth NJ, Craster RV. A consistent thin-layer theory for bingham plastics. Journal of Non-Newtonian Fluid Mechanics. 1999; 84:65–81.
11. Hewson RW, Kapur N, Gaskell PH. A model for film-forming with Newtonian and shear-thinning fluids. Journal of Non-Newtonian Fluid Mechanics. 2009; 162:21–28.
12. Afanasiev K, Munch A, Wagner B. Landau-Levich problem for non-Newtonian liquids. Physical Review E. 2007; 76:036307.
13. Perazzo CA, Gratton J. Thin film of non-Newtonian fluid on an incline. Physical Review E. 2003; 67
14. Balmforth N, Ghadge S, Myers T. Surface tension driven fingering of a viscoplastic film. Journal of Non-Newtonian Fluid Mechanics. 2007; 142:143–149.
15. Cook BP, Bertozzi AL, Hosoi AE. Shock solutions for particle-laden thin films. SIAM Journal on Applied Mathematics. 2008; 68:760–783.
16. Myers TG. Application of non-Newtonian models to thin film flow. Physical Review E. 2005; 72:066302–1–11.
17. Kheyfets VO, Kieweg SL. Experimental and numerical models of three-dimensional gravity-driven flow of shear-thinning polymer solutions used in vaginal delivery of microbicides. Journal of Biomechanical Engineering-Transactions of the ASME. 2013; 135:061009–1–14.
18. de Souza Mendes P, Marchesini F, Varges P. Gravity-driven azimuthal flow of a layer of thixotropic fluid on the inner surface of a horizontal tube. Journal of Non-Newtonian Fluid Mechanics. 2011; 166:1004–1011.
19. Weidner DE, Schwartz LW. Contact-line motion of shear-thinning liquids. Physics of Fluids. 1994; 6:3535–3538.
20. Braun RJ, Usha R, McFadden GB, Driscoll TA, Cook LP, King-Smith PE. Thin film dynamics on a prolate spheroid with application to the cornea. Journal of Engineering Mathematics. 2012; 73:121–138.

21. Tien D, Schnaare RL, Kang F, Cohl G, McCormick TJ, Moench TR, Doncel G, Watson K, Buckheit RW, Lewis MG, Schwartz J, Douville K, Romano JW. In vitro and in vivo characterization of a potential universal placebo designed for use in vaginal microbicide clinical trials. AIDS Res Hum Retroviruses. 2005; 21:845–53. [PubMed: 16225411]
22. Tasoglu S, Szeri AJ, Katz DF. Transport processes in vaginal films that release anti-HIV microbicide molecules. Biophysical Journal. 2011; 100:489–489. [PubMed: 21244845]
23. Acheson, DJ. Elementary Fluid Dynamics. Clarendon Press; Oxford: 2000. Oxford Applied Mathematics and Computing Science Series
24. Macosko, C. Rheology Principles, Measurements, and Applications. 4. Wiley-VCH; New York: 1994.
25. Kondic L. Instabilities in gravity driven flow of thin fluid films. SIAM Review. 2003; 45:95–115.
26. Kondic L, Diez J. Pattern formation in the flow of thin films down an incline: Constant flux configuration. Physics of Fluids. 2001; 13:3168–3184.
27. Diez JA, Kondic L, Bertozzi A. Global models for moving contact lines. Physical Review E. 2001; 63
28. Lin TS, Kondic L, Filippov A. Thin films flowing down inverted substrates: Three-dimensional flow. Physics of Fluids. 2012; 24
29. Huppert HE. Flow and instability of a viscous current down a slope. Nature. 1982; 300:427–429.
30. Diez JA, Kondic L. Contact line instabilities of thin liquid films. Physical Review Letters. 2001; 86:632–635. [PubMed: 11177899]
31. Bertozzi A, Brenner MP. Linear stability and transient growth in driven contact lines. Physics of Fluids. 1997; 9:530–539.
32. Craster RV, Matar OK. Dynamics and stability of thin liquid films. Reviews of Modern Physics. 2009; 81:1131–1198.
33. Spaid M, Homsy G. Stability of newtonian and viscoelastic dynamic contact lines. Physics of Fluids. 1996; 8:460–478.
34. Myers TG. Thin films with high surface tension. SIAM Review. 1998; 40:441–462.
35. Haeri S, Hashemabadi SH. Three dimensional CFD simulation and experimental study of power law fluid spreading on inclined plates. International Communications in Heat and Mass Transfer. 2008; 35:1041–1047.
36. Jerrett JM, Debruyn JR. Fingering instability of a gravitationally driven contact line. Physics of Fluids A-Fluid Dynamics. 1992; 4:234–242.

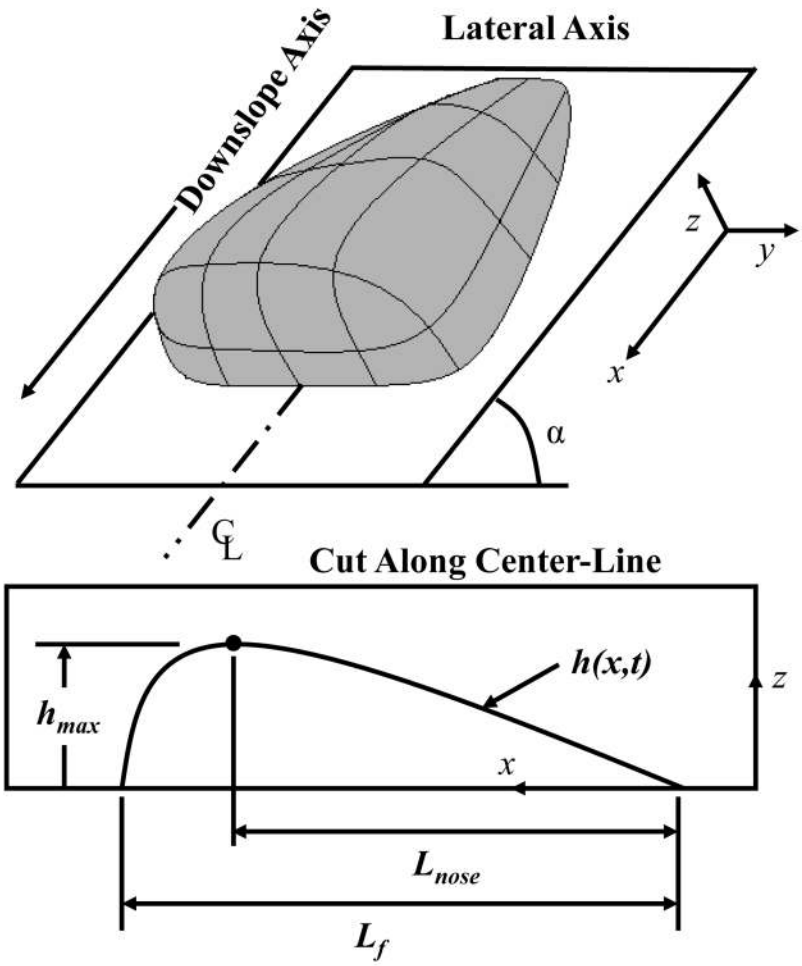

Figure 1. Coordinate System

Coordinate system and definitions of spreading characteristics in the *x* (downslope) and *y* (lateral) directions.

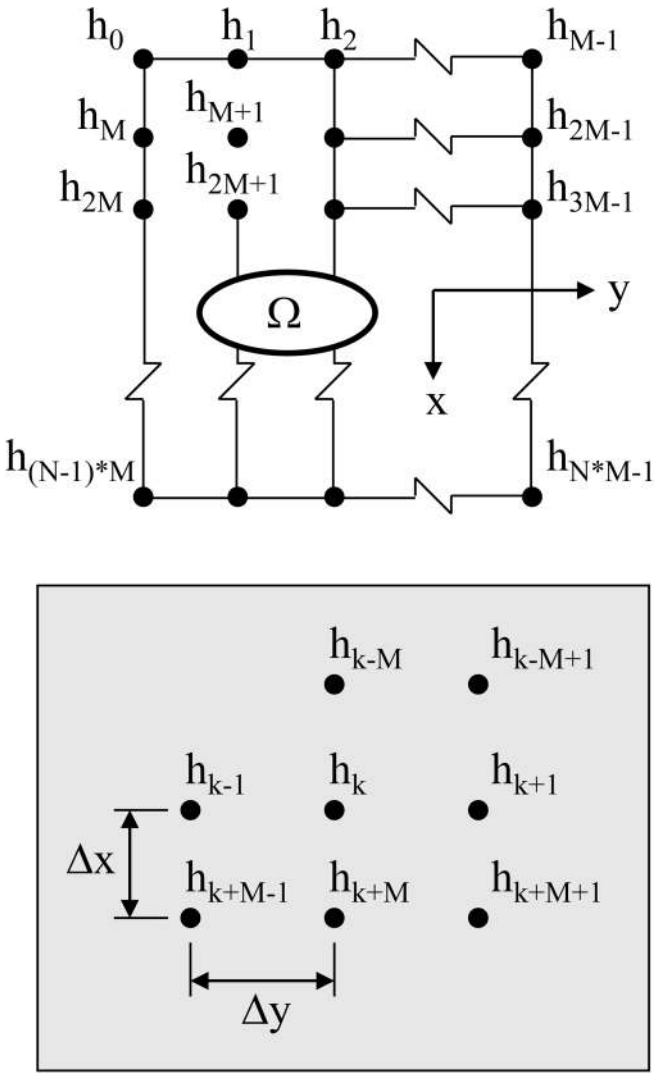

Figure 2. Domain (Ω) and computational stencil for the numerical method

The domain is divided into N points Δx distance apart in the downslope direction and M points Δy distance apart in the lateral direction.

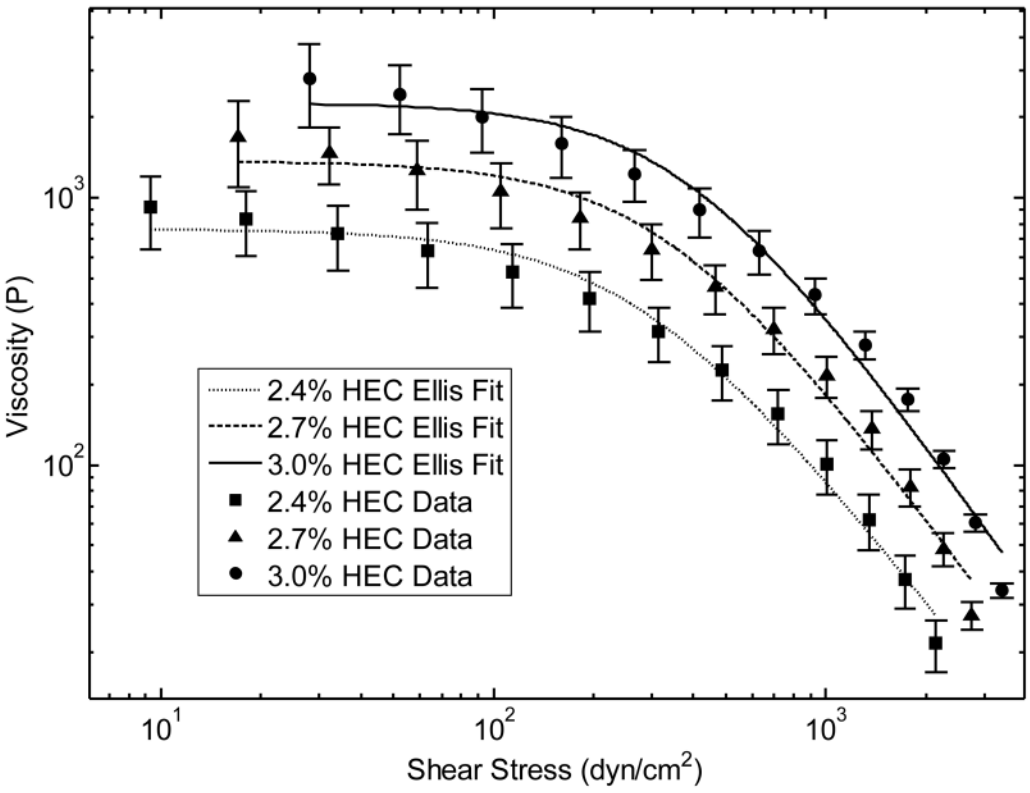

Figure 3. Example of rheological data for three hydroxyethylcellulose (HEC) solutions well-described by the Ellis constitutive equation

Lines indicate fit of the mean rheological data to the Ellis constitutive relationship (Eq. 5), with resulting parameters shown in Table 1. Rheology data were collected at 37 °C, on an AR 2000 Rheometer (TA Instruments), with a 40 *mm* 2 ° aluminum cone geometry. The data were collected in triplicate, and with a shear-rate sweep over 0.01 – 100/*s*, on a log scale sampling for three minutes at each shear rate. Bars indicate mean ± standard deviation of triplicate data.

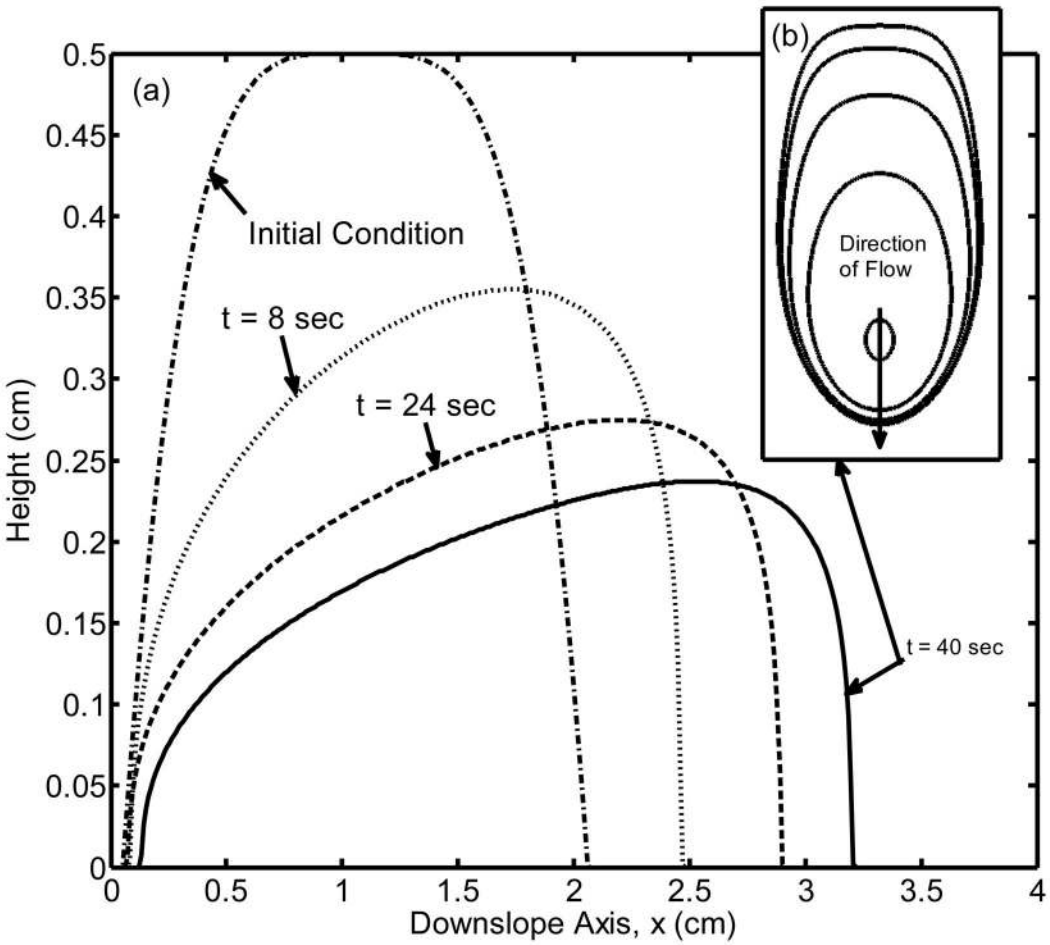

Figure 4. Example of spreading profiles at centerline cross-section and footprint view of numerical simulation

(a) Example side view spreading profile over time at centerline cross-section. **(b)** Top view of spreading footprint at $t = 40s$ with height contours drawn. Input parameters for simulation: $\alpha = 30\ °$, $\eta_0 = 1200P$ and $\tau_{1/2} = 200 dyn/cm^2$, and $\lambda = 1.2$.

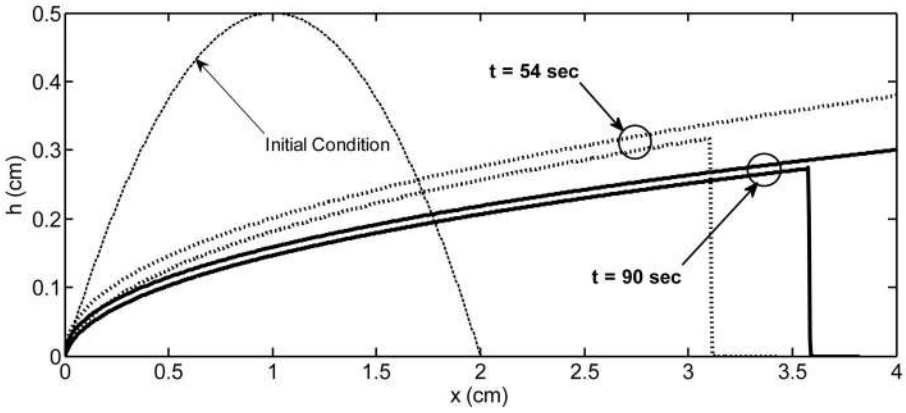

Figure 5. Comparison of similarity solution to numerical solution

Comparison of height profile, at $t = 54s$ (dashed gray) and $t = 90s$ (solid black) of spreading, obtained from the 3-D Ellis numerical solution and 2-D Ellis similarity solution. At each time point, the top curve represents the similarity solution, while the bottom curve represents a cross-section of the 3-D numerical solution, cut along its centerline. Agreement between the numerical and similarity solutions is improved as $t \to \infty$. Input parameters: $\alpha = 88\ °$, $\eta_0 = 3200P$, $\tau_{1/2} = 800 dyn/cm^2$, and $\lambda = 1.5$. Initial condition of shape: $h(x, y, t) = -0.5x^2 - 0.5y^2 + 0.5$. The steep inclination angle was used only in these simulations to compare to the similarity solution found for cases of $\cos\alpha \frac{\partial h}{\partial x} \ll 0$, as described in the Numerical Methods section. All other simulations in this study used $\alpha = 30\ °$.

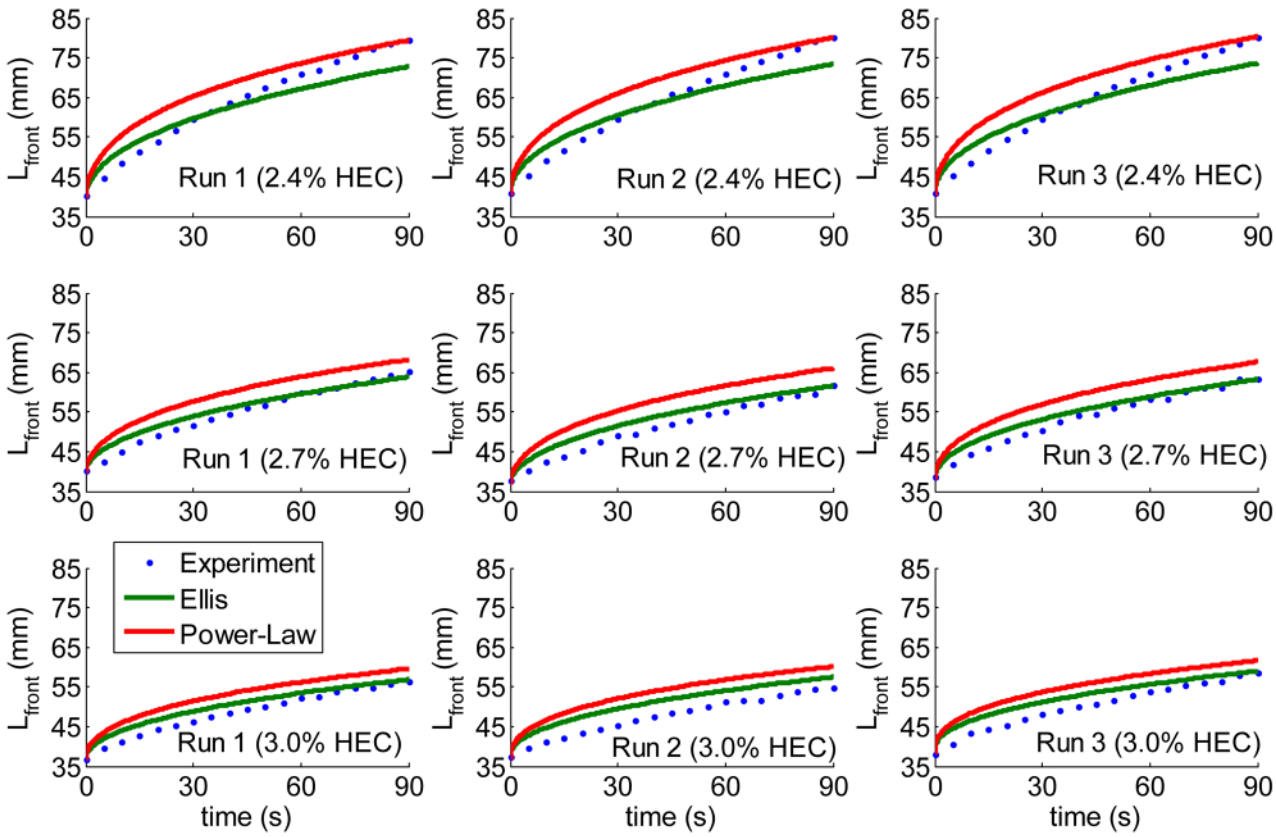

Figure 6. Comparison of numerical simulation to experiments

Down-slope spreading (L_{front}[=]cm) over time for the Ellis (green solid) and power-law (red solid) numerical simulations, compared against experiments. Power-law simulations and experimental results described in a previous study [17]. Nine experimental runs (three runs [R1, R2, R3] each of 2.4%, 2.7%, and 3.0% HEC concentration) are shown. The initial shape of the fluid for both simulations was created from the real initial shape from each experiment, as described in our previous study [17]. Qualitative assessment of the Ellis model shows improved agreement with the experiment over the power-law model.

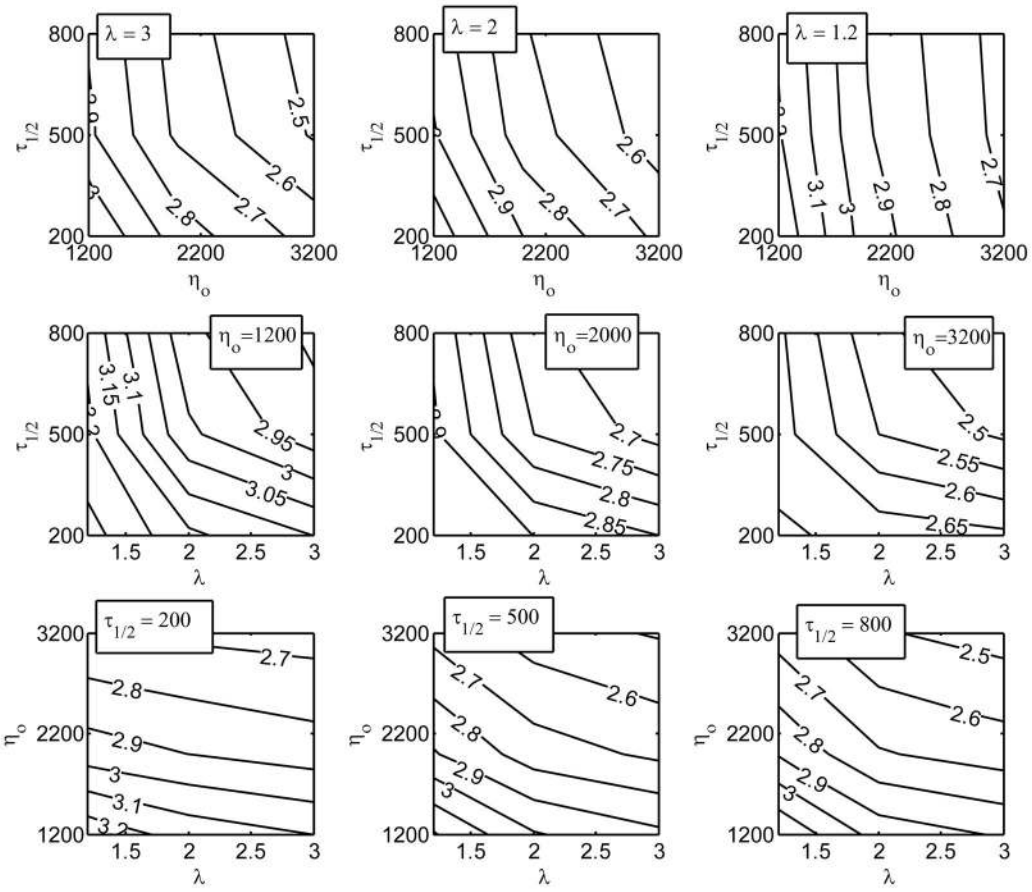

Figure 7. Contour plots of downslope spreading (L_{front}[=]*cm*) at *t* = 40s over Ellis parameter space

The *first row* shows a contour plot over a range of $\tau_{1/2}$ and η_0 for three values of λ. The *second row* shows a range of $\tau_{1/2}$ and λ at three values of η_0. The *third row* shows a range of η_0 and λ at three values of $\tau_{1/2}$. The contour lines on each plot were drawn from the corresponding nine simulations using a MATLAB interpolation for contours. Units: η_0[=]*P* and $\tau_{1/2}$[=]dyn/cm^2.

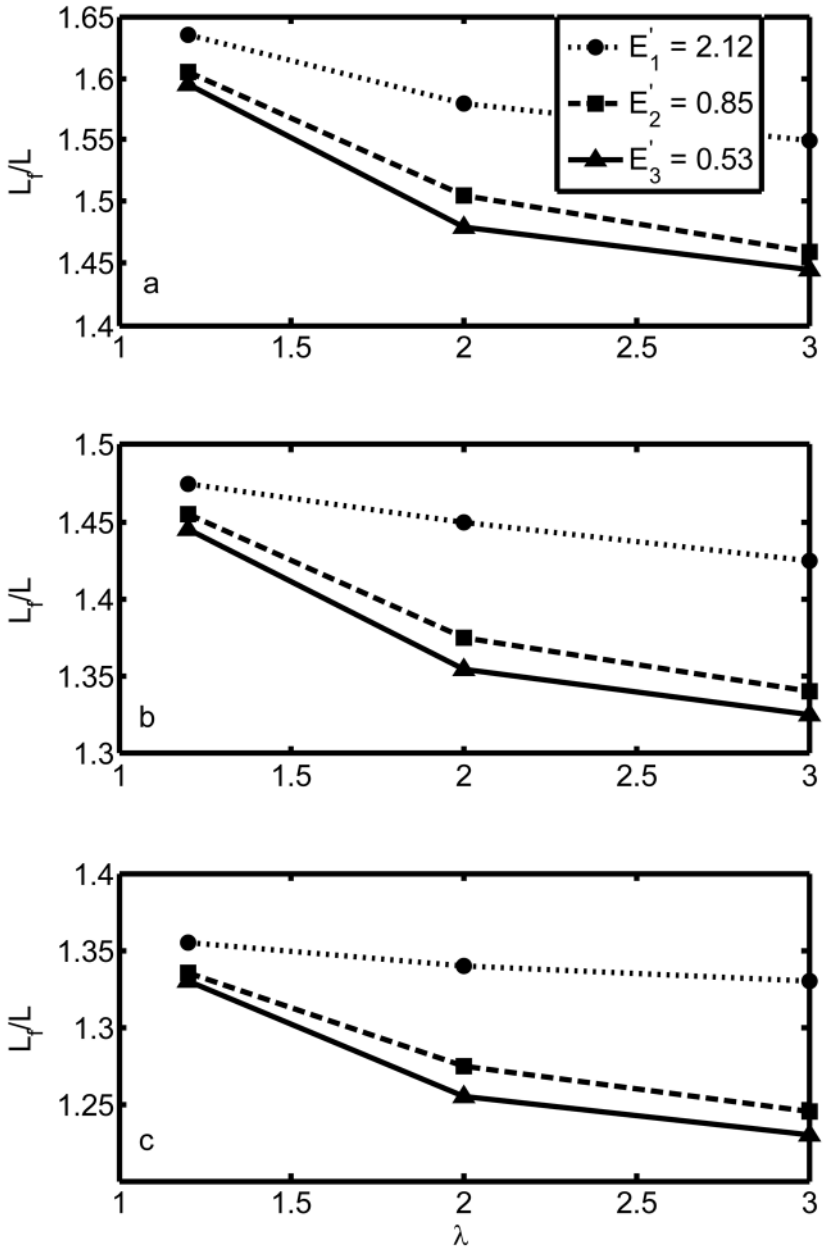

Figure 8. Dimensionless plots of downslope spreading as a function of dimensionless Ellis parameters

(a) $t' = 14.1$, **(b)** $t' = 8.49$, **(c)** $t' = 5.30$. Downslope spreading length = $L_{front} = L_f$ [=]cm, Initial length = $L = 2cm$, Dimensionless group $E' = \rho g H \cos \alpha / \tau_{1/2}$, Dimensionless group $t' = t/(\eta_0/\rho g H \cos \alpha)$. Only $t = 40s$ simulation data are shown.

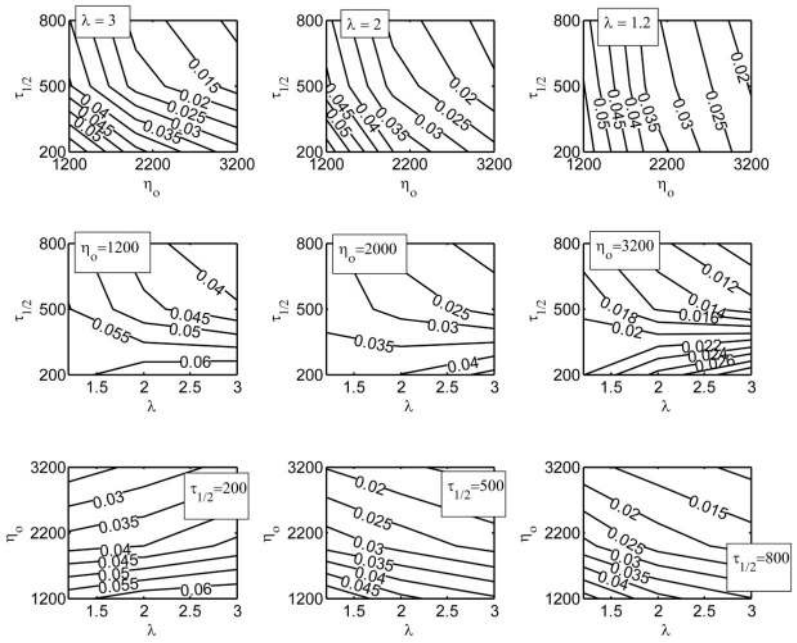

Figure 9. Contour plots of velocity saturation (*S*) over *t* = 40*s* over Ellis parameter space

As $S \to 0$, there was a more constant velocity, and less velocity saturation. The *first row* shows a contour plot over a range of $\tau_{1/2}$ and η_0 for three values of λ. The *second row* shows a range of $\tau_{1/2}$ and λ at three values of η_0. The *third row* shows a range of η_0 and λ at three values of $\tau_{1/2}$. The contour lines on each plot were drawn from the corresponding nine simulations using a MATLAB interpolation for contours. Units: $\eta_0[=]P$ and $\tau_{1/2}[=]dyn/cm^2$.

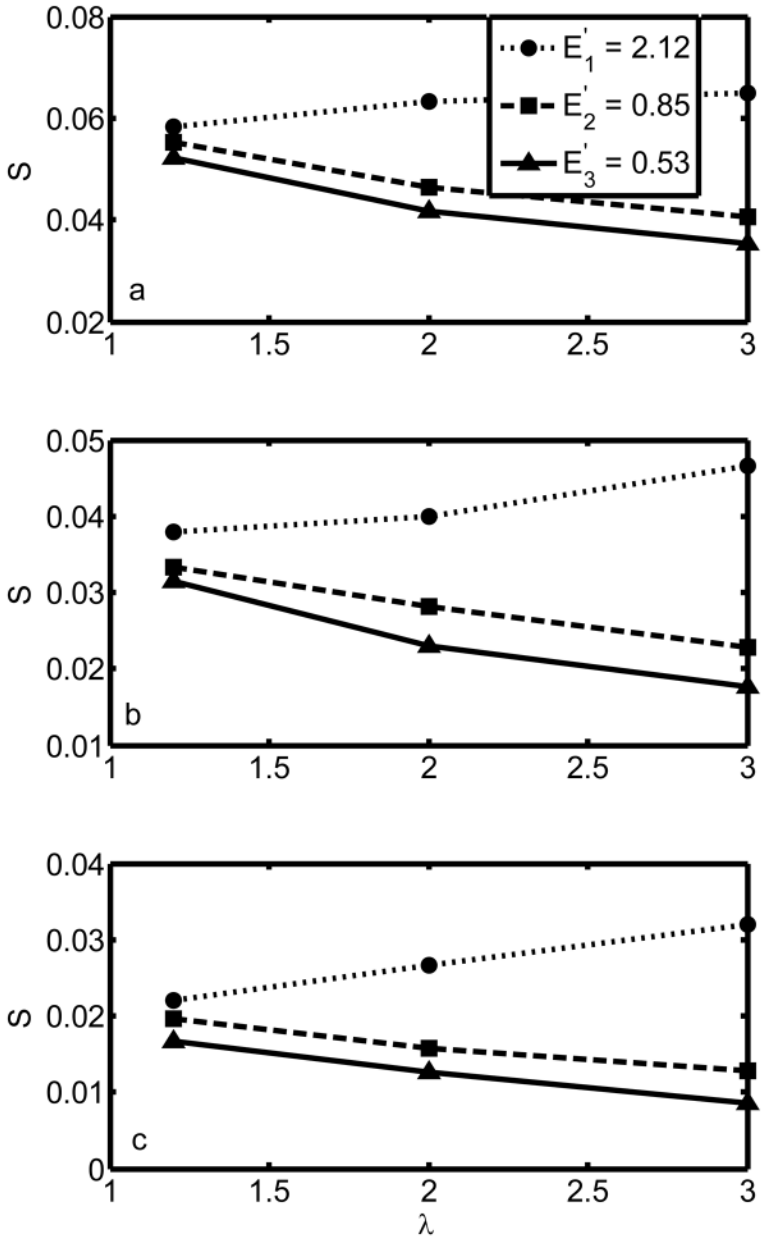

Figure 10. Dimensionless plots of velocity saturation as a function of dimensionless Ellis parameters

(a) $t' = 14.1$, **(b)** $t' = 8.49$, **(c)** $t' = 5.30$. Saturation parameter S defined in Eq. 34: $S \to 0$ when velocity is more constant, and S increases if the front velocity decelerates more. Dimensionless group $E' = \rho g H \cos \alpha / \tau_{1/2}$, Dimensionless group $t' = t/(\eta_0/\rho g H \cos \alpha)$. Only $t = 40s$ simulation data are shown.

Table 1

Rheological Parameters

Ellis parameters for three hydroxyethylcellulose (HEC) polymer solutions based on the 2.7% Universal Placebo [21]. R^2 values represent the goodness of fit of the mean rheological data (described and shown in Figure 3) to the Ellis constitutive relationship (Eq. 5).

HEC Concentration	$\eta_0(P)$	$\tau_{1/2}$ (dyn/cm^2)	λ	R^2
2.4%	762.56	276.98	2.604	0.9895
2.7%	1370.5	331.70	2.700	0.9888
3.0%	2264.9	381.00	2.800	0.9887

Table 2

Quantitative comparison between numerical simulations and experiment

RMS error between experiment and numerical simulations (either Ellis or power-law (PL)) of $L_{front}(mm)$ data over 90 s (shown in Figure 6). R1, R2, and R3 indicate the three experimental runs for each HEC concentration. The Ellis simulations result in lower RMS errors for all nine comparisons.

HEC Concentration:	**2.4%**		**2.7%**		**3.0%**	
Simulation Type:	**PL**	**Ellis**	**PL**	**Ellis**	**PL**	**Ellis**
Experiment R1	4.23	3.66	4.77	1.69	4.17	1.83
Experiment R2	4.71	3.45	5.92	2.26	5.71	3.28
Experiment R3	4.91	3.35	5.07	1.64	4.68	2.38